DOI: 10.1002/chem.201103095

Synthesis, Structural Characterization, Photophysics, and Broadband Nonlinear Absorption of a Platinum(II) Complex with the 6-(7-Benzothiazol-2′-yl-9,9-diethyl-9*H*-fluoren-2-yl)-2,2′-bipyridinyl Ligand

Bingguang Zhang,[a] Yunjing Li,[a] Rui Liu,[a] Timothy M. Pritchett,[b] Alexander Azenkeng,[c] Angel Ugrinov,[a] Joy E. Haley,[d] Zhongjing Li,[a] Mark R. Hoffmann,[e] and Wenfang Sun*[a]

Abstract: A platinum complex with the 6-(7-benzothiazol-2′-yl-9,9-diethyl-9*H*-fluoren-2-yl)-2,2′-bipyridinyl ligand (**1**) was synthesized and the crystal structure was determined. UV/Vis absorption, emission, and transient difference absorption of **1** were systematically investigated. DFT calculations were carried out on **1** to characterize the electronic ground state and aid in the understanding of the nature of low-lying excited electronic states. Complex **1** exhibits intense structured $^1\pi$–π^* absorption at $\lambda_{abs} < 440$ nm, and a broad, moderate ^{1}MLCT/^{1}LLCT transition at 440–520 nm in CH_2Cl_2 solution. A structured $^3\pi$–π^*/^{3}MLCT emission at about 590 nm was observed at room temperature and at 77 K. Complex **1** exhibits both singlet and triplet excited-state absorption from 450 nm to 750 nm, which are tentatively attributed to the $^1\pi$–π^* and $^3\pi$–π^* excited states of the 6-(7-benzothiazol-2′-yl-9,9-diethyl-9*H*-fluoren-2-yl)-2,2′-bipyridine ligand, respectively. *Z*-scan experiments were conducted by using ns and ps pulses at 532 nm, and ps pulses at a variety of visible and near-IR wavelengths. The experimental data were fitted by a five-level model by using the excited-state parameters obtained from the photophysical study to deduce the effective singlet and triplet excited-state absorption cross sections in the visible spectral region and the effective two-photon absorption cross sections in the near-IR region. Our results demonstrate that **1** possesses large ratios of excited-state absorption cross sections relative to that of the ground-state in the visible spectral region; this results in a remarkable degree of reverse saturable absorption from **1** in CH_2Cl_2 solution illuminated by ns laser pulses at 532 nm. The two-photon absorption cross sections in the near-IR region for **1** are among the largest values reported for platinum complexes. Therefore, **1** is an excellent, broadband, nonlinear absorbing material that exhibits strong reverse saturable absorption in the visible spectral region and large two-photon-assisted excited-state absorption in the near-IR region.

Keywords: luminescence · nonlinear optics · photophysics · platinum · two-photon absorption

Introduction

Square-planar platinum(II) complexes have drawn great attention in the last two decades because of the intriguing photophysical properties and the resulting, versatile, potential applications in photonic devices, such as in organic light-emitting diodes (OLEDs),[1] dye-sensitized solar cells,[2] photochemical cells,[3] and optical sensors.[4] These applications are essentially based on the complexes' long-lived phosphorescence at room temperature, moderate to strong metal-to-ligand charge transfer absorption in the visible spectral region, and multiple intramolecular charge-transfer transitions. More importantly, these properties can be modulated by chemical or physical stimuli, such as pH, temperature, cation, anion, and so forth.[4] In recent years, our group and several other groups have reported the potential of utilizing the broad and moderately strong excited-state absorption of some platinum complexes in the visible to the near-IR region for nonlinear optical applications, including optical switching and laser-pulse compression.[5]

[a] Dr. B. Zhang, Dr. Y. Li, Dr. R. Liu, Dr. A. Ugrinov, Z. Li, Dr. W. Sun
Department of Chemistry and Biochemistry
North Dakota State University, Fargo, ND 58108-6050 (USA)
Fax: (+1) 701-231-8831
E-mail: Wenfang.Sun@ndsu.edu

[b] Dr. T. M. Pritchett
US Army Research Laboratory, AMSRD-SE-EM
2800 Powder Mill Road, Adelphi, MD 20783-1197 (USA)

[c] Dr. A. Azenkeng
Energy and Environmental Research Center
University of North Dakota, Grand Forks, ND 58202-9018(USA)

[d] Dr. J. E. Haley
Materials and Manufacturing Directorate
Air Force Research Laboratory
Wright Patterson Air Force Base, Dayton, OH 45433 (USA)

[e] Dr. M. R. Hoffmann
Department of Chemistry
University of North Dakota, Grand Forks, ND 58202-9024(USA)

Supporting information for this article is available on the WWW under http://dx.doi.org/10.1002/chem.201103095.

 © 2012 Wiley-VCH Verlag GmbH & Co. KGaA, Weinheim

Another attractive feature of square-planar Pt^{II} complexes is the ease of structural modification. A variety of monodentate, bidentate, terdentate, and tetradentate ligands have been reported to coordinate with the platinum ion.[6] Photophysical properties of the resultant complexes are drastically modulated by the different types of ligands. Among the various ligands, terpyridyl and 6-phenyl-2,2′-bipyridyl (C^N^N) ligands have been widely investigated.[6a] It has been shown that due to the π-donating ability of the phenyl ring and reduced distortion from the square-planar configuration in the 6-phenyl-2,2′-bipyridyl platinum complexes, the [Pt(C^N^N)] complexes exhibit stronger emission than the corresponding platinum terpyridyl complexes. Studies in our group further revealed that the [Pt(C^N^N)] complexes exhibit broader triplet excited-state absorption in the visible to the near-IR region and stronger reverse saturable absorption at 532 nm for ns laser pulses than the terpyridyl counterparts.[5a,d,l,p,r] Therefore, [Pt(C^N^N)] complexes are promising broadband nonlinear-transmission materials. By introducing electron-donating alkoxyl substituents on the phenyl ring of the C^N^N ligand, the lowest excited state incorporates more intraligand-charge-transfer character, leading to a longer triplet excited-state lifetime and enhanced emission.[5l]

Recently, we reported that incorporation of a π-donating fluorenyl substituent on the 4-position of the central pyridine ring of the C^N^N ligand increased the triplet-excited-state lifetimes, the emission quantum yields, and the ratios of the excited-state absorption cross-section relative to that of the ground-state for these complexes.[5r] Consequently, stronger reverse saturable absorption was observed from the platinum(II) chloride complex containing the 4-fluorenyl substituent on the central pyridine ring than in the corresponding complexes without the fluorenyl substituent.[5r] Intrigued by these results, we are interested in how the photophysics and nonlinear absorption would be influenced by introducing the substituted fluorenyl component at the 6-position of the pyridine ring to form a new type of C^N^N ligand. In addition, incorporating the fluorenyl component into the platinum complex would greatly improve the probability of two-photon absorption (TPA) of the complex in the near-IR region; thus allowing for the possibility to populate the excited state through TPA. In earlier studies, we found that [Pt^{II}(C^N^N)] complexes exhibit broadband excited-state absorption that extends from the visible to the near-IR region.[5a,d,l,p,r] However, the lack of ground-state absorption above 570 nm prevents population of the excited state through one-photon absorption; this limits the potential application of these complexes as broadband nonlinear absorbing materials. If the excited state could be populated through TPA, it would not only allow the utilization of the broadband excited-state absorption, but the TPA itself could also reduce the transmission of light.

Other important structural modifications include introduction of the benzothiazolyl (BTZ) substituent on the fluorene unit. Because the BTZ group is an electron-withdrawing aromatic component, it would not only extend the π conjugation in the target molecule, that is, complex **1** in Scheme 1, but also make the complex possess the acceptor (BTZ)–π (fluorenyl component)–acceptor (bipyridinyl Pt component) (A–π–A) feature. The A–π–A structural feature has been found to be an effective approach to enhance TPA in organic molecules.[7] Previous studies by our group and by others have demonstrated that Pt^{II} complexes containing the BTZ-substituted fluorenyl acetylide ligands exhibit broadband TPA in the near-IR region.[5q,t] By taking all these factors into consideration, complex **7** in Scheme 1 was initially designed. However, due to the limited solubility of **7** in organic solvent, the chloride ligand in **7** was replaced by the 4-tolylacetylide ligand to improve the solubility. Thus, complex **1** in Scheme 1 became the target complex in this study, and its synthesis, crystal structure, photophysics, and TPA are reported herein.

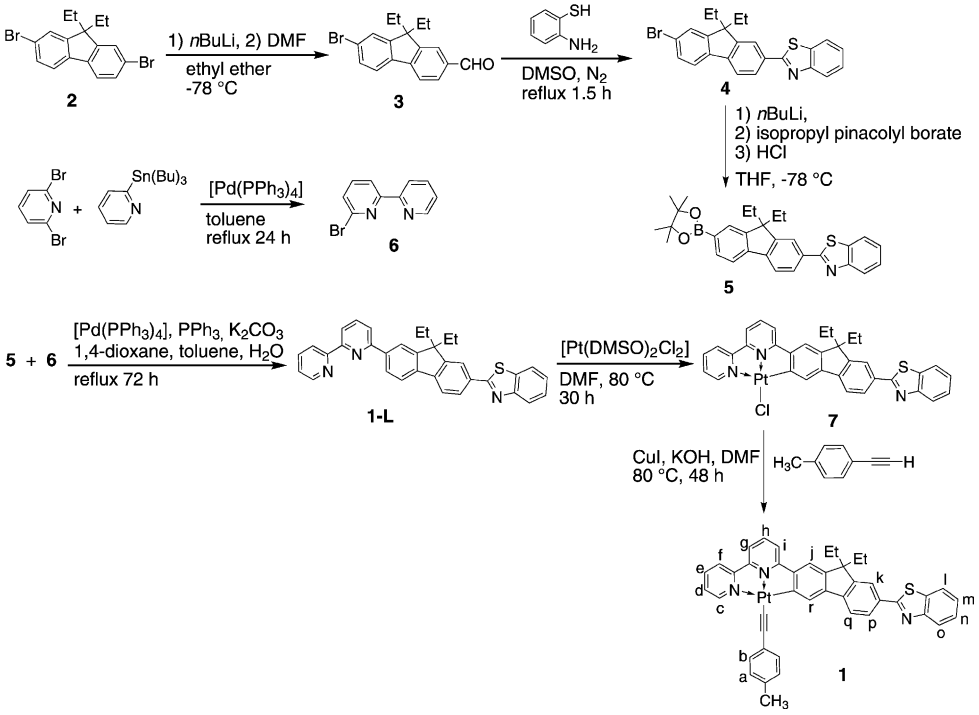

Scheme 1. Synthetic route for **1**.

Because the ultimate goal of our research is to optimize the reverse saturable absorption of platinum complexes, it is

 © 2012 Wiley-VCH Verlag GmbH & Co. KGaA, Weinheim

critical to understand the photophysical parameters that influence the reverse saturable absorption. Key characteristics of an ideal reverse saturable absorber include: 1) considerable ground-state absorption to enable population of the excited state; 2) high excited-state quantum yield; 3) long excited-state lifetime that exceeds the excitation pulse width; and 4) most importantly, the excited-state absorption should be much stronger than the ground-state absorption, that is, the ratio of the excited-state absorption cross section relative to that of the ground state should be significantly larger than 1. The ground-state absorption cross section can be deduced from the electronic absorption measurement, whereas the excited-state absorption characteristics need to be obtained from the transient difference absorption measurements. Emission measurements would provide information on the energy level and the lifetime of the excited state. Quantitative characterizations of the excited-state absorption and TPA cross sections in this study were achieved by performing the *Z*-scan experiments and the data were fitted by using a five-level model. Nonlinear transmission measurements at 532 nm were conducted to demonstrate the reverse saturable absorption of the complex in response to ns laser pulses.

Results and Discussion

Synthesis: The precursor compounds **2**, **3**, **4**, and **6** were synthesized according to the procedures reported in the literature. Lithiation of **4** in dry THF at low temperature, followed by reaction with isopropyl pinacolyl borate gave the key precursor **5** in 70% yield.[8] Suzuki coupling reaction between **5** and **6** led to the formation of ligand **1-L** in 70% yield. The cyclometalated platinum(II) chloride complex **7** was prepared by following the reported procedures for [Pt(C^N^N)Cl] complexes from the ligand **1-L** and [Pt(DMSO)$_2$Cl$_2$] in DMF, in which a few drops of water was added as catalyst to activate the C–H bond.[9] Although complex **7** was obtained in a very high yield, the solubility of **7** was so poor that it could not be further purified and characterized. Therefore, it was used directly, without further purification, in the following step to prepare **1**. The target complex **1** was synthesized by replacing the chloride ligand by 1-ethynyl-4-methylbenzene in DMF with KOH as base for deprotonation of 1-ethynyl-4-methylbenzene and a catalytic amount of CuI to facilitate the substitution reaction.[5d,10] The resultant complex **1** shows much better solubility than chloride complex **7**. It is soluble in CH_2Cl_2, $CHCl_3$, acetonitrile, acetone, DMF, and DMSO; and slightly soluble in methanol and ethanol.

The new compound/complex **1-L** and **1** were fully characterized by ^{1}H NMR spectroscopy, HRMS, and elemental analyses. High-quality single crystals of **1-L** and **1** suitable for X-ray crystallography were also obtained by slow diffusion of heptane vapor to dilute CH_2Cl_2 solutions of the sample. The crystal structures for **1-L** and **1** will be discussed in the following section.

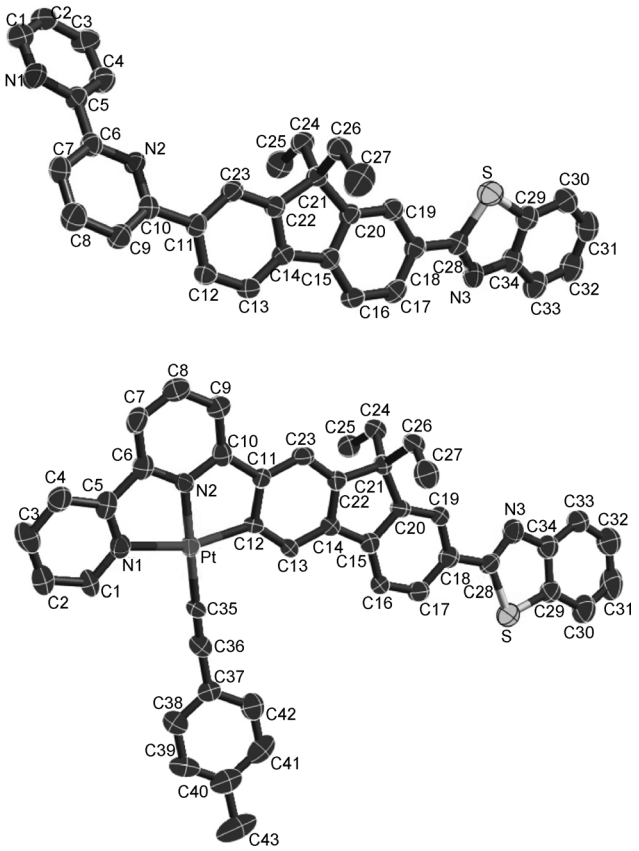

Figure 1. ORTEP view of **1-L** (top) and **1** (bottom; with 50% probability for thermal ellipsoids). Hydrogen atoms are omitted for clarity.

Crystal structures of 1-L and 1: Figure 1 shows an ORTEP view of the crystal structures of ligand **1-L** and complex **1**; with selected bond lengths and angles listed in Table 1 and Table 2. The full list of bond lengths and bond angles for **1-**

Table 1. Selected bond lengths (Å) for **1** and **1-L**.

Atom1	Atom2	**1** XRD	Calcd[a]	**1-L** XRD
Pt	N1	2.112(8)	2.189	
Pt	N2	1.980(7)	2.025	
Pt	C12	1.997(8)	1.996	
Pt	C35	2.00(1)	1.963	
S	C28	1.757(9)	1.794	1.748(3)
S	C29	1.711(9)	1.750	1.724(3)
N1	C1	1.37(1)	1.339	1.337(4)
N1	C5	1.36(1)	1.363	1.342(3)
N2	C6	1.35(1)	1.349	1.345(3)
N2	C10	1.36(1)	1.359	1.344(3)
N3	C28	1.32(1)	1.299	1.318(4)
N3	C34	1.39(1)	1.380	1.395(3)
C5	C6	1.49(1)	1.484	1.490(3)
C10	C11	1.49(1)	1.466	1.488(3)
C11	C12	1.44(1)	1.437	1.397(4)
C12	C13	1.40(1)	1.397	1.377(4)
C14	C15	1.46(1)	1.461	1.466(3)
C18	C28	1.48(1)	1.465	1.466(3)
C20	C21	1.53(1)	1.534	1.526(4)
C21	C22	1.55(1)	1.534	1.528(2)
C35	C36	1.18(1)	1.228	
C36	C37	1.46(1)		

[a] From DFT/LANG631 calculations.

 © 2012 Wiley-VCH Verlag GmbH & Co. KGaA, Weinheim

Table 2. Selected bond angles (°) for **1** and **1-L**.

Atom1	Atom2	Atom3	**1** XRD	Calculated[a]	**1-L** XRD
Pt	N1	C1	125.9(6)	127.3	
Pt	N1	C5	113.9(6)	112.7	
Pt	N2	C6	120.7(6)	119.9	
Pt	N2	C10	118.2(6)	116.3	
Pt	C12	C11	111.9(6)	112.4	
Pt	C12	C13	130.0(6)	129.4	
Pt	C35	C36	176.8(9)	177.5	
S	C28	N3	115.6(7)	114.6	115.5(2)
S	C28	C18	122.2(7)	121.2	121.6(2)
S	C29	C34	110.0(7)	109.2	109.7(2)
N1	Pt	C12	160.3(3)	159.2	
N1	Pt	C35	102.0(3)	102.0	
N1	C5	C6	115.1(8)	116.0	116.8(2)
N2	Pt	C12	82.3(3)	81.9	
N2	Pt	C35	178.9(3)	179.2	
N2	Pt	N1	78.0(3)	77.2	
N2	C6	C5	112.0(8)	114.2	115.5(2)
N2	C10	C11	111.5(7)	113.1	115.9(2)
N3	C28	C18	122.1(8)	124.1	122.9(2)
N3	C34	C29	115.0(9)	115.4	115.2(2)
C10	C11	C12	116.0(7)	116.3	121.8(2)
C12	Pt	C35	97.7(3)	98.9	
C17	C18	C28	121.1(8)	118.7	119.2(2)
C19	C18	C28	118.8(8)	118.7	121.7(2)
C28	S	C29	89.6(4)	88.7	89.5(1)
C28	N3	C34	109.8(8)	112.1	110.0(2)
C35	C36	C37	173(1)	179.2	

[a] From DFT/LANG631 calculations.

L and **1** are provided in the Supporting Information, Tables S1 and S2. The X-ray structure of **1-L** indicates that the two pyridine rings that adopt a *trans* conformation are not coplanar, with a dihedral angle of 13.16° between them. Both pyridine rings are twisted out of the plane of fluorene, with dihedral angles of 43.86° and 18.62° relative to the fluorene plane for the end pyridine ring and the middle pyridine ring, respectively. In addition, the benzothiazole group is not coplanar with the fluorene plane either. A dihedral angle of 17.18° is displayed between these two components. The C28–S bond length is 1.748(3) Å and that of C29–S is 1.724(3) Å. The C–N bond lengths in the pyridine rings are similar, generally around 1.34 Å. However, those in the benzothiazole component are significantly different (i.e., 1.318(4) Å and 1.395 Å). The C28-S-C29 bond angle is close to 90°.

After coordination with Pt^{II}, the bipyridine and fluorene components become almost coplanar. The dihedral angle between the plane of the bipyridinyl–Pt^{II} component (defined by Pt, N1, C1, C2, C3, C4, C5, C6, C7, C8, C9, C10, and N2 atoms) and the fluorene plane (defined by C11, C12, C13, C14, C15, C16, C17, C18, C19, C20, C21, C22, and C23 atoms) is 3.39°; whereas the dihedral angle between the plane of the bipyridinyl–Pt^{II} component and the benzothiazole plane (defined by the nine atoms of benzothiazole (N3, C28, S, C29, C30, C31, C32, C33, C34)) is 15.56°. Between the fluorene component and the benzothiazole component, the dihedral angle is 18.65°. The toluene plane is twisted by 17.65° from the plane of the bipyridinyl–Pt^{II} component. In contrast, the Pt atom lies almost in the same plane as the bipyridinyl–Pt^{II} plane, with a deviation of 0.020 Å from the plane. The bond lengths around Pt^{II} are 2.112(8) Å for Pt–N1, 2.00(1) Å for Pt–C35, 1.997(8) Å for Pt–C12, and 1.980(7) Å for Pt–N2. The longer Pt–N1 distance could possibly arise from a strong *trans* influence from the fluorene C donor at the *trans* position. The bond angles around Pt^{II}, which are 82.3(3)° for N2-Pt-C12, 78.0(3)° for N1-Pt-N2, 102.0(3)° for N1-Pt-C35, and 97.7(3)° for C12-Pt-C35, deviate somewhat from the ideal square-planar configuration angle (90°). In general, the bond lengths and bond angles around the Pt^{II} atom are consistent with those reported for other [Pt^{II}(C^N^N)] and Pt^{II} terpyridyl complexes.[11]

Figure 2 shows the 3D packing of **1**, with the two neighboring molecules stacked parallel to each other in a head-to-head but back-to-back fashion. The shortest distance between two neighboring Pt atoms is 3.867 Å, which is slightly longer than the metal–metal interaction distance (3.09–3.50 Å) usually observed in extended, linear-chain-arranged, monomeric, Pt^{II} structures.[12] Therefore, no intermolecular Pt–Pt interactions are expected from complex **1** even in the solid state. However, the distances between two adjacent layers are approximately 3.4 Å, which would allow for strong intermolecular Pt–π and π–π interactions to occur. The presence of intermolecular Pt–π and π–π interactions was also supported by ^{1}H NMR analysis of **1** at various concentrations, as discussed in detail in the next section. Note that such interactions would alter the electronic structure of the complex in the solid state and make it quite different from those in the gas phase or in a solution. However, because all of the photophysical properties and nonlinear absorption of **1** discussed in this paper are investigated in solutions, consideration of the solid-state electronic properties is not only less important, but also beyond the scope of this work.

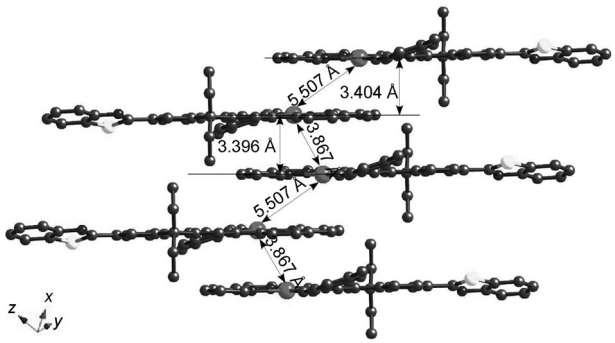

Figure 2. 3D packing of **1**. The distances between neighboring planes, defined by Pt, N1, C1, C2, C3, C4, C5, C6, C7, C8, C9, C10, and N2 atoms, are as follows: 3.396 Å if the Pt–Pt distance is 3.867 Å, and 3.430 Å if the Pt–Pt distance is 5.507 Å. These distances represent π–π interaction between bipyridine fragments.

^{1}H NMR spectrum of 1: Figure 3 shows the aromatic region of the ^{1}H NMR spectra of **1** in $CDCl_3$ at different concentrations. The assignment of the peaks in the spectrum is based on the chemical shift and the splitting pattern. Hydrogen

 © 2012 Wiley-VCH Verlag GmbH & Co. KGaA, Weinheim

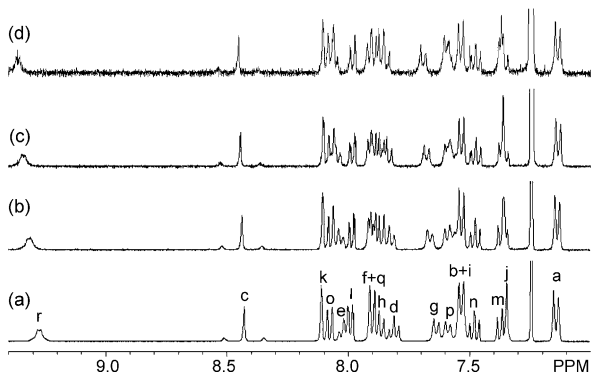

Figure 3. ^{1}H NMR spectra of complex **1** at different concentrations in $CDCl_3$: a) 1.0×10^{-2}, b) 5.0×10^{-3}, c) 2.5×10^{-3}, d) 1.0×10^{-3} mol L^{-1}.

atoms c and r (for labels see Scheme 1), which are at the *ortho* positions of the coordinating atoms on the terminal pyridine ring, and the fluorene ring are most deshielded due to the reduced electron density on the respective carbon atoms after coordination of the pyridine and phenyl rings with Pt^{II}. With increased concentration of the solution, the peaks corresponding to protons r, c, d, e, f, g, h, i, and j shift to high field. The up-field shift appears to be indicative of significant intermolecular π–π interactions at high concentrations. The head-to-head stacking pattern observed in the crystal structure analysis indicates that the C^N^N components are on top of each other between the neighboring molecules, thus placing the C^N^N component of **1** in the shielding zone of the aromatic rings on the other molecule, which results in the up-field shift of the protons on the C^N^N ligand.

DFT calculations: DFT calculations were performed to characterize the ground electronic state of complex **1** and low-lying singlet excited states. The optimized structure of **1** in the gas phase is shown in the Supporting Information, Figure S1, and selected bond lengths and bond angles are given in Table 1 and Table 2 together with those obtained from X-ray crystallography analysis for comparison. Figure 4 shows the ground-state electron-density distribution of the five HOMOs (HOMO, HOMO−1, HOMO−2, HOMO−3, and HOMO−4) and the five LUMOs (LUMO, LUMO+1, LUMO+2, LUMO+3, and LUMO+4) for complex **1**. The relative contributions of the ligand/metal fragments to HOMO−1, HOMO, LUMO and LUMO+1 are listed in Table 3. Table 4 lists the excitation energies (eV), wavelengths (nm), oscillator strengths, and coefficients of dominant contributing configurations of ten, low-lying, singlet, electronic states of complex **1** based on time-dependent DFT (TDDFT) calculations at the MPW3LYP/LANG631 level of theory.

Table 3. Contribution of fragments to the frontier molecular orbitals (FMOs) in complex **1**.

Fragment	Contribution (%)			
	HOMO−1	HOMO	LUMO	LUMO+1
Bipyridine	10.48	1.69	92.26	49.37[a]
Pt	15.52	21.14	5.53	1.35
Tolylacetylide	2.56	76.67	1.27	0
BTZ-F2	71.44	0	0.94	49.31

[a] This value is falsely similar to that for the BTZ-F2 fragment because of an artifact in the calculation that stem from the apparently large atomic-orbital coefficients of a few atoms in the bipyridine fragment. The correct prediction is shown qualitatively in the MO plots in Figure 4, in which the electron density of LUMO+1 is predominantly located on the BTZ-F2 fragment.

Results of ground-state properties show that the calculated bond lengths and angles are generally in good agreement with those obtained from X-ray crystal analysis (see Table 1 and Table 2). The largest difference between the calculated and observed bond lengths is 0.077 Å for the distance between the Pt atom and N1 atom, whereas the smallest devia-

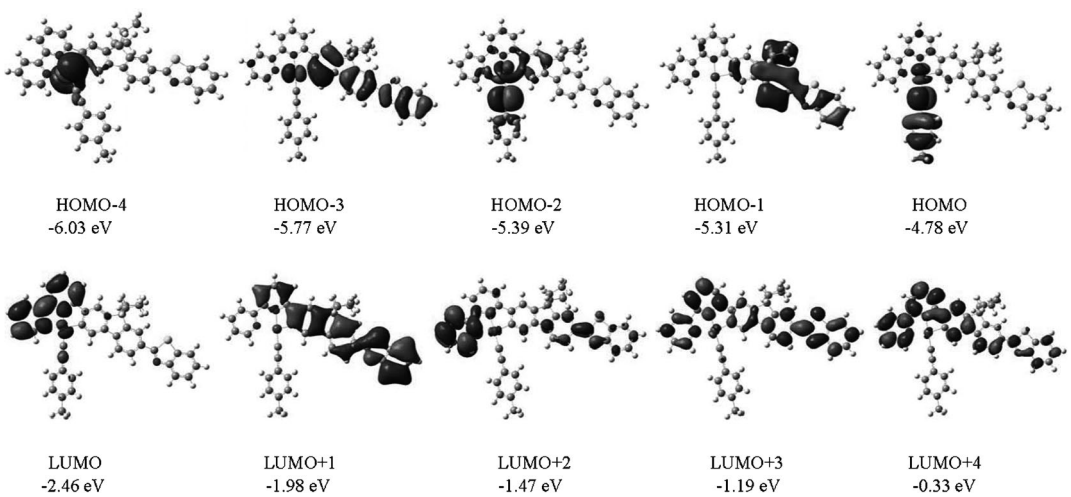

Figure 4. Contour plots of the five HOMOs (HOMO−1, HOMO−2, HOMO−3, HOMO−4) and the five LUMOs (LUMO, LUMO+1, LUMO+2, LUMO+3, LUMO+4) for complex **1**.

 © 2012 Wiley-VCH Verlag GmbH & Co. KGaA, Weinheim

Table 4. Excitation energies, wavelengths, oscillator strengths, dominant contributing configuration, and the associated configuration coefficient of ten low-lying electronic states (S_n) of complex **1** obtained at the MPW3LYP/LANG631[a] level of theory.

S_n	Excitation energy [eV]	[nm]	f	Dominant configuration	Configuration coefficient
1	1.84	673	0.0591	HOMO→LUMO	0.67
2	2.25	550	0.0098	HOMO−2→LUMO	0.64
3	2.29	541	0.0016	HOMO−1→LUMO	0.63
4	2.36	526	0.0591	HOMO→LUMO+1	0.64
5	2.67	464	0.0015	HOMO−4→LUMO	0.70
6	2.78	447	0.0089	HOMO→LUMO+2	0.53
7	2.79	444	0.0081	HOMO−3→LUMO	0.46
8	2.83	438	0.0885	HOMO−2→LUMO+1	0.60
9	2.95	420	0.5445	HOMO−1→LUMO+1	0.47
10	3.21	386	0.0715	HOMO→LUMO+4	0.67

[a] LANG631 basis set refers to 6-31G* for C, H, N and S and LANL2DZ for Pt.

tion is 0.001 Å for the Pt–C12 bond. Although the X-ray structure depicts the Pt–N1 connection with a solid bond, calculations show a rather nonbonded interaction as shown in Figure S1 in the Supporting Information, with bond order significantly less than a single bond. The Wiberg bond index for this bond, based on natural bond orbital (NBO) analysis[13] calculations, is determined to be only 0.23. The large difference between the calculated and measured Pt–N1 distance could be just an artifact in the DFT calculations. Alternatively, it could be due to the lack of consideration of intermolecular interactions in the DFT calculations. Deviations in bond angles range from 0 to 6.2°; with the largest difference observed for the C35-C36-C37 angle in the 4-tolylacetylide ligand, for which the experimental value is 173° and the calculated value is 179.2°. The benzene ring on the acetylide ligand is found to be twisted away from the molecular plane by about 11°. This additional strain in the acetylide ligand can be expected to contribute to the slightly larger deviation seen in the C35-C36-C37 angle. The mean absolute deviation (MAD) from the experimental bond lengths is 0.020 Å, whereas that for bond angles is 1.2°. The molecule is so large that theoretical calculations that employ a larger basis set than 6-31G* for atoms other than Pt were computationally unfeasible. Slight differences from the X-ray crystallography data can be expected because theoretically predicted geometrical parameters are generally sensitive to the basis set size. Even though the inclusion of relativistic effects through the effective core potential of Pt is helpful, it is far from complete. In addition, theoretical calculations were performed for molecules in the gas phase in vacuo and do not take into account the interactions that occur in solid-state compounds used in the X-ray crystallography experiments.

To understand the nature of the low-lying, excited, singlet, electronic states of complex **1**, TDDFT calculations were performed. The results shown in Table 4 indicate that electronic transitions to the first excited state involve the HOMO→LUMO orbital pair as the dominant contributing configuration and occurs at 673 nm, whereas the HOMO→LUMO+1 transition is the dominant contributing configuration to the fourth excited state, which occurs at 526 nm. For the transition at 420 nm, which has the strongest oscillator strength (i.e., the ninth excited state), the dominant contributing configuration involves the HOMO−1→LUMO+1 orbital pair. Excitations to the second, third, and fifth excited states emanate from deeper-lying MOs, that is, HOMO−2, HOMO−1 and HOMO−4, respectively, and have small oscillator strengths. According to the electron-density distribution analysis, the electron density of the LUMO is almost exclusively localized on the bipyridine component (92%), with about 6% on Pt (d orbitals) and only about 1% each on the 4-tolylacetylide and BTZ-F2 components. The HOMO shows a very different electron-density distribution pattern, with about 77% contribution from the 4-tolylacetylide fragment, 21% from the Pt (d orbitals) and about 2% from bipyridine; whereas the contribution from the BTZ-F2 component is zero. In contrast, the HOMO−1 has dominant contribution from the BTZ-F2 fragment and considerable contributions from the metal and bipyridine components; with a small contribution of about 2.6% from 4-tolylacetylide. The distribution on the LUMO+1 is almost evenly split between the bipyridine and BTZ-F2 components; the metal adds only approximately 1% of the electron density and the contribution from 4-tolylacetylide is zero. Overall, the contribution from Pt (d orbitals) is largest in the HOMO and HOMO−1 (21.1% and 15.5%, respectively), small but important in the LUMO, whereas it is marginal in the LUMO+1 (see Table 3). Therefore, the dominant transitions that contribute to the three major transitions at 673, 526, and 420 nm are Pt(dπ)+tolylacetylide(π)→bpy(π*), Pt(dπ)+tolylacetylide(π)→BTZ-F2(π*)+bpy(π*), and BTZ-F2(π)→BTZ-F2(π*)+bpy(π*) transitions, respectively.

Based on theoretical calculations, the lowest-energy electronic transition (which is the HOMO→LUMO as expected) should correspond to the lowest-energy absorption band maximum in the measured UV/Vis absorption spectrum. However, the experimental absorption band maximum was observed at 459 nm, whereas the value predicted from calculations was 673 nm; this represents an overestimation of about 200 nm. The experimental value was obtained in a polar solvent (CH_2Cl_2), which can usually cause the lowest-energy absorption band maximum to be hypsochromically shifted. Generally, energetic parameters that are determined based on differences in the total electronic energy are sensitive to both theoretical method and basis set size. Therefore, part of the deviation can be explained by the fact that a relatively small basis set of 6-31G* for C, N, S, and H atoms in conjunction with LANL2DZ for the Pt atom was used for computing the properties of complex **1**; as noted earlier, the molecule is large and calculations with a larger basis set were not computational feasible. In addition, the theoretical prediction is based on gas-phase calculations in vacuo with no consideration of solvent effects, whereas experimental measurements were conducted in the condensed phase in CH_2Cl_2. Although polarized continuum model

 © 2012 Wiley-VCH Verlag GmbH & Co. KGaA, Weinheim

(PCM) calculations are often used in theoretical calculations to account for solvation effects, the molecule considered in this study was large and such calculations were not feasible. Even if the above-mentioned effects were allowed, the deviation of the TDDFT result (i.e., 0.86 eV) is larger than typical for TDDFT descriptions of excitations that are local in nature (i.e., typically 0.2–0.3 eV) and provide an important clue that the excitation has Rydberg or charge-transfer character (i.e., errors in the 1–2 eV range are not uncommon). Consequently, although the predicted value of the absorption band maximum represents a semi-quantitative estimate, TDDFT calculations still provide valuable information on the electronic structure of the lowest excited states; this is useful in interpreting and understanding the photophysics observed for complex **1** described in the following sections.

Electronic absorption: The electronic absorption of **1-L** and **1** obeys the Beer–Lambert law in the concentration range used in our study (5×10^{-6}–5×10^{-3} mol L^{-1}, see the Supporting Information, Figure S2). The UV/Vis absorption spectra of **1-L** and **1** in CH_2Cl_2 are shown in Figure 5. The absorption band maxima and molar extinction coefficients are presented in Table 5. The absorption of **1-L** is dominated by structured bands in the UV region, which emanate from the $^1\pi$–π^* transitions. The polarity of solvent exhibits minor effect on the UV/Vis spectrum of **1-L** (see the Supporting Information, Figure S3 a), which is consistent with the $^1\pi$–π^* assignment. For complex **1**, the dominant absorption also appears in the UV region, however, the bands are redshifted compared with those in **1-L**, indicating the delocalization of the ligand-centered molecular orbitals through interactions with the platinum dπ orbitals; this is consistent with observations from the DFT study. Considering the similarity in energy of these bands for **1** and **1-L** and the large molar extinction coefficients of these bands in **1**, we can assign these bands to $^1\pi$–π^* transitions within the 6-(7-benzothiazol-2′-yl-9,9-diethyl-9*H*-fluoren-2-yl)-2,2′-bipyridine ligand (predominantly within the benzothiazolylfluorene component as predicted by the DFT calculations) as well. In addition, a broad, structureless tail between 430 and 530 nm is observed in complex **1**, but not in ligand **1-L**. With reference to other Pt^{II} C^N^N and terpyridyl acetylide complexes, this tail could be attributed to the ^{1}MLCT/^{1}LLCT (metal-to-ligand/ligand-to-ligand charge transfer) transitions. The assignment of this low-energy absorption band is bolstered by DFT calculations, in which the HOMO is dominated by the tolylacetylide ligand and the Pt components, and the LUMO has major contribution from the bipyridine component (see Table 3). Another piece of evidence that supports the charge transfer nature of the low-energy absorption band is the negative solvatochromic effect. As demonstrated in the Supporting Information, Figure S4, this band shifts to a longer wavelength in less polar solvents, such as toluene and hexane, in comparison with the bands in more polar solvents (CH_3CN, CH_2Cl_2 and DMSO). This is indicative of the charge-transfer character of the ground state.

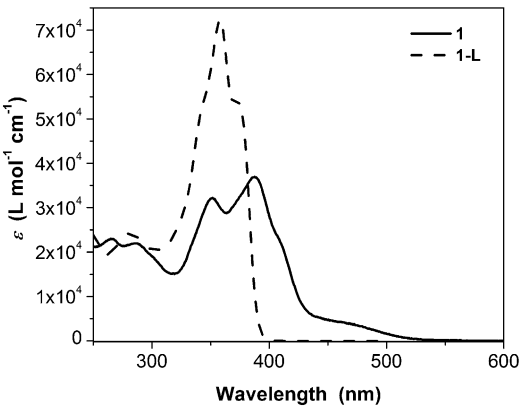

Figure 5. UV/Vis absorption spectra of **1-L** and **1** in CH_2Cl_2.

Emission: **1-L** and **1** are both emissive in solutions at room temperature and in glassy matrix at 77 K. As shown in Figure 6, upon excitation of **1-L** at 356 nm in CH_2Cl_2 solution, it exhibits structured emission at 380 and 410 nm, which decays with a lifetime of 752 ps. The quantum yield of the emission is 73%. Because of the mirror relationship between the emission spectrum and the UV/Vis absorption spectrum and the lifetime, the observed emission from **1-L** is attributed to fluorescence from the $^1\pi$–π^* state. The assignment of the $^1\pi$–π^* state as the emitting state of **1-L** is supported by the minor solvent effect. As shown in the Supporting Information, Figure S5, in different solvents with a broad range of polarity, the emission energies and quantum yields (except in hexane) are quite similar. The only difference is the relative intensity of the vibronic peaks.

For complex **1**, upon excitation at 388 nm, a broad, somewhat structured emission appears at 591 nm with a shoulder

Table 5. Photophysical parameters of **1-L** and **1**.

	λ_{abs} [nm][a] (logε [M^{-1}cm^{-1}])	λ_{em} [nm][b] (Φ_{em}; τ_0)	λ_{em} [nm] (τ/μs)[c]	$\lambda_{S_1-S_n}$ [nm] (τ_S/ps)[d]	$\lambda_{T_1-T_n}$ [nm] ($\varepsilon_{T_1-T_n}$ [M^{-1}cm^{-1}]; τ_{TA}/μs; Φ_T)[e]
1-L	282 (4.39), 358.5 (4.86), 373 (4.73)	380, 410 (0.73; 752 ps)	379, 402 (0.011 (16%), 0.090 (84%)), 427, 453	646 (796±96)	585 (83290; 32.8; 0.36)[f]
1	265 (4.36), 286 (4.34), 352 (4.51), 387.5 (4.57), 458 (3.63)	591 (0.067; 1.43 μs), 634 (–; 1.38 μs)	575 (19.4), 625 (21.1)	633 (24.6±14.8)	633 (44650; 14.0; 0.28)[g]

[a] UV/Vis absorption band maxima and molar extinction coefficients in CH_2Cl_2. [b] Emission-band maximum, quantum yield, and lifetime in CH_2Cl_2 at a concentration of 5×10^{-6} mol L^{-1}. [c] Emission-band maxima and lifetime in a butyronitrile matrix at 77 K at a concentration of 5×10^{-6} mol L^{-1}. [d] Femtosecond transient difference absorption (fs TA) band maximum and singlet excited-state lifetime in CH_2Cl_2. [e] ns TA band maximum, triplet extinction coefficient, triplet excited-state lifetime and quantum yield. [f] Measured in butyronitrile. [g] Measured in CH_2Cl_2. SiNc in C_6H_6 was used as the reference. (ε_{590} = 70000 L mol^{-1}cm^{-1}, Φ_T = 0.20).

 © 2012 Wiley-VCH Verlag GmbH & Co. KGaA, Weinheim

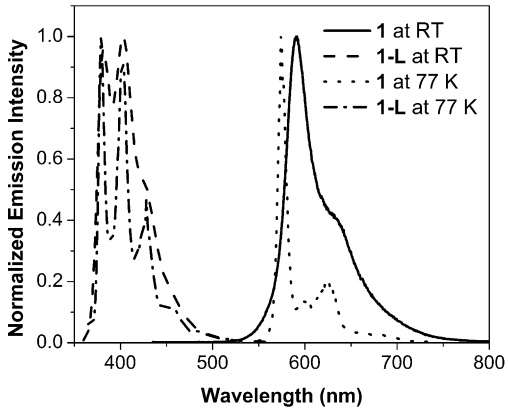

Figure 6. Normalized emission spectra of **1-L** and **1** in CH_2Cl_2 solutions at room temperature and in butyronitrile matrix at 77 K for **1**.

at approximately 634 nm. The vibronic spacing between the peak and the shoulder is approximately 1150 cm^{-1}, corresponding to the ring-breathing mode of the aromatic rings in the ligands. The lifetime of the emission is approximately 1.43 μs. In view of the large Stokes shift of the emission and the long lifetime, the emission from **1** at room temperature should originate from a triplet excited state. The vibronic structure in the emission spectrum suggests that the $^3\pi$–π^* state should be involved in the emission, possibly mixed with some ^{3}MLCT character; this is partially supported by the negative solvatochromic effect of the emission (see the Supporting Information, Figure S5). In less polar solvents, such as in toluene and hexane, the emission spectra are redshifted and become less structured in contrast to those in more polar solvents, such as ethanol, acetonitrile, CH_2Cl_2, and acetone. This probably is indicative of different degrees of mixing the ^{3}MLCT character into the $^3\pi$–π^* state in solvents with different polarities. In polar solvents, the less polar ^{3}MLCT state (in comparison to the more polar MLCT ground state) is less stabilized than the ground state; this would cause the blueshift of the ^{3}MLCT emission. In contrast, the influence of the solvent polarity on the $^3\pi$–π^* excited state is not as significant as that on the ^{3}MLCT state. This would allow for the ^{3}MLCT state and the $^3\pi$–π^* state to be energetically more close to each other in polar solvents, resulting in more configurational mixing of $^3\pi$–π^* and ^{3}MLCT characters in the emission in polar solvents. On the other hand, in less polar solvents, the ^{3}MLCT state would be more stabilized and the energy level would be lowered, whereas the energy of the $^3\pi$–π^* state is less affected. Consequently, the energy gap between these two states becomes larger and the contribution from the $^3\pi$–π^* state is reduced. This is reflected by the less structured emission spectra and shorter lifetime in less polar solvents (see the Supporting Information, Table S3). When the concentration of the CH_2Cl_2 solution increases from 1×10^{-6} to 1×10^{-4} mol L^{-1}, the intensity of the emission keeps increasing (see the Supporting Information, Figure S6) and the lifetime remains the same, suggesting that no self-quenching occurs in the concentration range used herein.

The emission spectra of **1-L** and **1** in butyronitrile matrix at 77 K are given in Figure 6. For **1-L**, the emission spectrum at 77 K exhibits clear vibronic structures, but remains at the same energy as that at room temperature, and the lifetime is shorter than 100 ns. Therefore, it is still fluorescence from the $^1\pi$–π^* state. Our attempt to measure the phosphorescence at 77 K was unsuccessful even if we added an excess amount of CH_3I to the solution. The emission spectrum of **1** at 77 K becomes narrower and blueshifted compared with that at room temperature; this is due to the rigidochromic effect.[14] The vibronic spacing is approximately 1390 cm^{-1}, which is also consistent with the stretching vibration of the aromatic ligand. Considering the small thermally induced Stokes shift ($\Delta E_s \cong 470$ cm^{-1}), the similar shape and vibronic spacing of the spectra at 77 K and at room temperature for **1**, the emission of **1** at 77 K is tentatively assigned as the $^3\pi$–π^* state, possibly mixed with some ^{3}MLCT character.

Transient absorption spectroscopy: Transient difference absorption spectroscopy measures the difference between the excited-state absorption and the ground-state absorption. Thus, it can provide information on the spectral region in which the excited-state absorption is stronger than that of the ground-state and predict the wavelength region in which reverse saturable absorption could occur. From the decay of the transient absorption, the lifetime of the excited state that gives rise to the excited-state absorption is obtained. This is especially important for measuring the singlet excited-state lifetime of the Pt^{II} complexes that cannot be obtained from the decay of fluorescence because of the lack of fluorescence at room temperature in many cases. By estimating the triplet excited-state molar extinction coefficient at the triplet excited-state absorption band maximum with the singlet depletion method,[15] and by using the relative actinometry,[16] with SiNc in benzene as the reference, the triplet excited-state quantum yield can be obtained. Both the singlet and triplet transient difference absorption spectra of **1-L** and **1** were measured with fs and ns pump-probe UV/Vis spectrometers, respectively.

Figure 7 shows the time-resolved singlet transient difference absorption spectra of **1-L** and **1** in CH_2Cl_2. For **1-L**, immediately after the excitation at 400 nm with ultrafast femtosecond laser pulses (150 fs), a broad, slightly structured absorption band appears at about 650 nm, which decays rapidly and redshifts to about 675 nm. At longer decay time, a new broad band occurs at approximately 580 nm, accompanied by an isosbestic point at 480 nm. This reflects the intersystem crossing from the singlet excited state to the triplet excited state. The spectrum at longer delay times is consistent with that measured by ns laser flash photolysis (shown in Figure 8). The singlet lifetime measured from the decay of fs TA is quite similar to that obtained from fluorescence decay (see Table 5). Therefore, the observed singlet TA is attributed to the $^1\pi$–π^* state, whereas the TA at long decay time should arise from the $^3\pi$–π^* state. For complex **1**, the fs TA spectra changes very little in the whole spectrometer decay window (6 ns) although it exhibits a very

 © 2012 Wiley-VCH Verlag GmbH & Co. KGaA, Weinheim

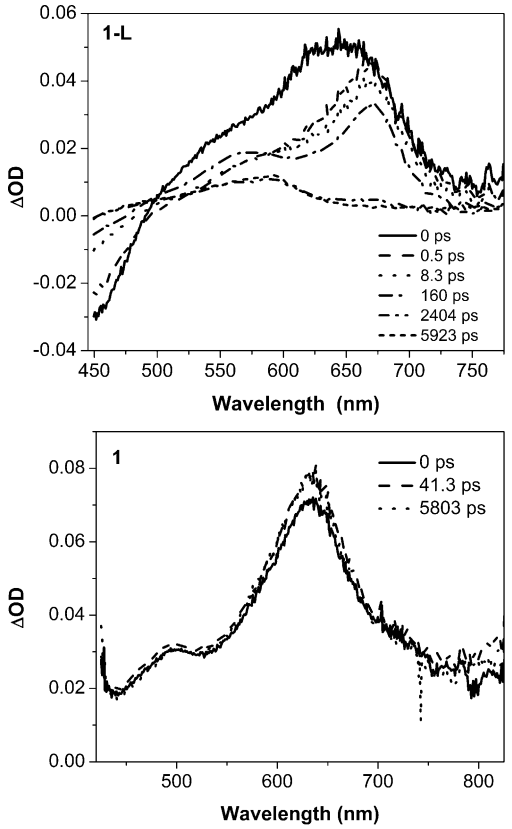

Figure 7. Time-resolved singlet transient difference absorption spectra of **1-L** (top) and **1** (bottom) in CH_2Cl_2. $\lambda_{ex}=400$ nm.

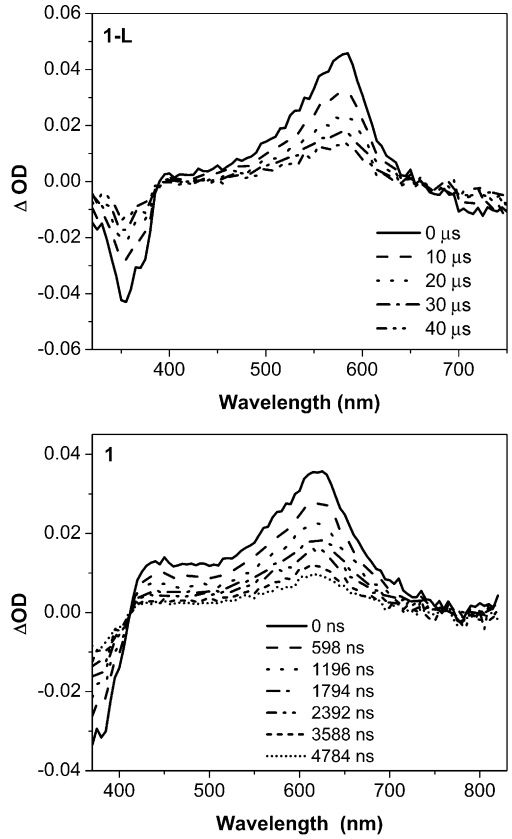

Figure 8. Time-resolved triplet transient difference absorption spectra of **1-L** (top) in butyronitrile and **1** (bottom) in CH_3CN. $\lambda_{ex}=355$ nm.

small change right after the excitation, which correlates to a lifetime of approximately 25 ps. We assume that this is due to a decay of the singlet excited state, including intersystem crossing to the triplet excited state. At longer decay time, the spectrum is essentially the same as that measured by ns flash photolysis and is attributed to the triplet excited-state absorption. Because there is not much difference in the spectral properties of the singlet and triplet excited states, we can assume that the geometry of the molecule does not change much upon intersystem crossing. In addition, the TA spectrum of **1** is quite similar to that of **1-L**, therefore, the singlet excited state that contributes to the observed TA could be assigned as the $^1\pi$–π^* and the triplet state as the $^3\pi$–π^* as well. However, the singlet lifetime of the Pt complex **1** is much shorter compared with that of the ligand **1-L**. This is attributed to the increased intersystem crossing through spin-orbital coupling through Pt; this makes the decay of the singlet excited state more rapid.

The time-resolved triplet transient difference absorption spectra of **1-L** in butyronitrile and **1** in CH_3CN are presented in Figure 8. The ns TA spectra of **1** in CH_2Cl_2 and toluene are provided in the Supporting Information, Figure S7. The spectral features for **1-L** and **1** are quite similar, with a positive absorption band appearing in the visible spectral region and a bleaching band below 400 nm for **1-L** and below 415 nm for **1**. However, the spectrum of **1** is redshifted compared with that of **1-L**, which is reflected by the absorption band maximum, that is, 620 nm for **1** and 585 nm for **1-L**. The redshifted TA spectrum of **1** compared with that of **1-L** suggests delocalization of the ligand-centered molecular orbitals through interactions with the platinum dπ orbitals; this is similar to that observed in the UV/Vis absorption spectrum for the singlet excited state. A similar feature has been reported for platinum diimine complex with acetylide ligands.[17] The extinction coefficients at the band maximum, the lifetimes deduced from the decay of the transient absorption, and the triplet excited-state quantum yield determined from relative actinometry for **1-L** in butyronitrile and **1** in CH_2Cl_2 are listed in Table 5 (the data for **1** in CH_2Cl_2, rather than those in CH_3CN, are listed because we need to use the triplet excited-state parameters in CH_2Cl_2 to fit the *Z*-scan data measured in CH_2Cl_2 solution). The triplet extinction coefficients for both **1-L** and **1** are quite large, accompanied by long triplet lifetimes. The long lifetime of 32.8 μs for **1-L** implies that the transient absorption likely arises from the $^3\pi$–π^* state. For complex **1**, although the lifetime (14.0 μs in CH_2Cl_2) of the excited state that gives rise to the transient absorption is shorter than that of the ligand, probably due to the increased decay from T_1 to S_0 by spin-orbital coupling through Pt, or possibly because the reduced energy level of the $^3\pi$–π^* excited state (evident by the redshifted TA band) in **1** leads to reduced lifetimes according to the energy-gap law,[18] it is still much longer than that deduced from the decay of emission. This

 © 2012 Wiley-VCH Verlag GmbH & Co. KGaA, Weinheim

indicates that the transient species would likely arise from the $^3\pi$–π^* state and is supported by the similar features of the TA spectra of **1** and **1-L**. The assignment of the absorbing excited state in CH_2Cl_2 solution to $^3\pi$–π^*, rather than the ^{3}MLCT state or a mixed state, is also partially based on the fact that the lifetimes deduced from the decay of TA in toluene (13.5 μs) is similar to that in CH_2Cl_2. This phenomenon is distinct from the solvent-dependency lifetime deduced from the decay of emission, in which the emitting state has different composition of $^3\pi$–π^*/^{3}MLCT character with varied solvent polarity. Therefore, we conclude that the excited state that gives rise to the transient absorption in CH_2Cl_2 and toluene solutions is the ligand-centered $^3\pi$–π^* state that is not affected pronouncedly by the polarity of solvents. However, in more polar, coordinating solvent, such as CH_3CN, the lifetime (2.0 μs) deduced from the decay of the transient absorption is much shorter than those in CH_2Cl_2 and toluene solutions, suggesting that the ^{3}MLCT state plays a role in transient absorption in CH_3CN solution.

***Z*-scan study and nonlinear absorption cross sections**: *Z* scan[19] is a simple, nonlinear-optical, characterization technique that is used to separately measure the contributions of nonlinear absorption and nonlinear refraction to the observed optical nonlinearity of a material, with nonlinear absorption evaluated by open-aperture *Z*-scan measurement. In general, nonlinear absorption is dominated by the singlet excited-state absorption if the intersystem crossing time of the molecule is longer than the laser pulse width. In contrast, triplet excited-state absorption plays the major role when the intersystem crossing time is shorter than the laser pulse width. Therefore, the observed nonlinear absorption often is a combination of singlet and triplet excited-state absorption. In the case of a molecule that exhibits TPA at the excitation wavelength, two-photon initiated excited-state absorption would contribute to the observed open-aperture *Z*-scan data. To separate the contribution of singlet excited-state absorption from triplet excited-state absorption, and the contribution of TPA from excited-state absorption (in the near-IR region), open-aperture *Z* scans were performed in a CH_2Cl_2 solution at 532 nm by using both ns and ps laser pulses and at a variety of visible and near-IR wavelengths by using ps pulses. The experimental data were then fitted by using the five-level model described previously[5g,n,q,s,20] with the input parameters (σ_0, τ_s, τ_T, Φ_T) obtained from the photophysical studies described above to abstract both the singlet and triplet excited-state absorption cross sections (σ_s and σ_T) and the TPA cross sections (σ_2). Representative *Z*-scan data and fitting curves are provided in Figure 9. Table 6 lists the resulting values of the excited-state absorption cross sections at wavelengths in the visible region, together with the ratio of the excited-state absorption cross section relative to that of the ground-state; also shown in Table 6 are the values of the TPA cross sections in the near-IR region.

The data in Table 6 show that the excited-state absorption cross sections at all of the wavelengths studied are in the range of 10^{-17} to 10^{-16} cm^2, which is comparable to, or even larger than, those reported in the literature for other reverse saturable absorbers.[5,21] The combination of strong excited-state absorption and weak ground-state absorption in the visible and near-IR regions leads to large ratios of the excited-state to ground-state absorption cross sections. The ratio becomes extremely large at longer wavelengths; this places it among the largest ratios reported to date for reverse saturable absorbers. Comparisons of the ratios of **1** to those of other reported compounds are provided in the Supporting Information, Tables S4 and S5. It is obvious that the ratios of **1** are larger than most of the reported reverse saturable absorbers. Although the ratios of **1** are smaller than those for platinum 2,2′-bipyridine complexes with 2-(benzothiazol-2′-yl)-9,9-diethyl-7-ethynylfluorene ligands at multiple wavelengths,[5q] the reverse saturable absorption spectral region for **1** (430–680 nm) is broader than that for the platinum 2,2′-bipyridine complex (450–600 nm). This feature along with the large absorption cross-section ratios, as well as the long triplet excited-state lifetime makes complex **1** a very promising broadband reverse saturable absorber.

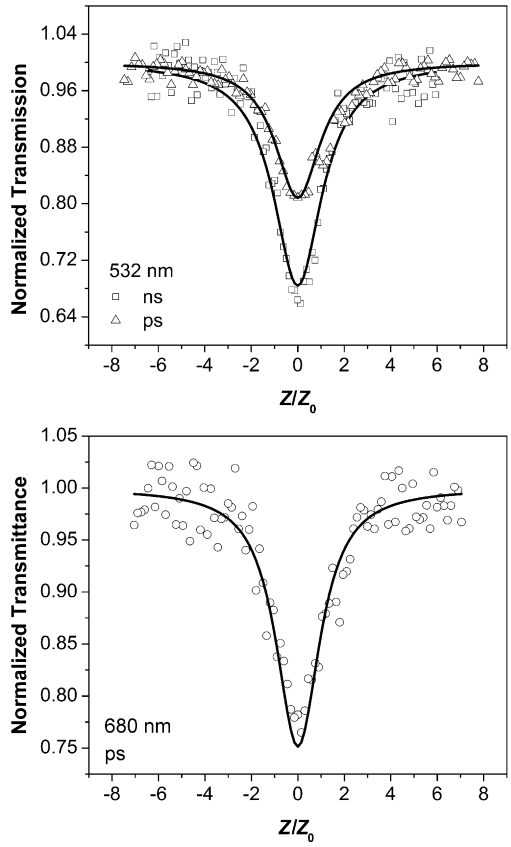

Figure 9. Plots of *Z*-scan experimental data (symbols) and fitting curves (solid lines) for **1** in CH_2Cl_2 solution at 532 (top) and 680 nm (bottom) in a 2 mm cell. The spot size at the focal plane is 33 μm for ps pulses and 37 μm for ns pulses at 532 nm, and 38 μm for ps pulses at 680 nm. The energy used is 5.2 μJ for ns measurement and 3.1 μJ for ps measurement at 532 nm, and 10.7 μJ for ps measurement at 680 nm. The solution concentration is 6.72×10^{-4} and 3.82×10^{-4} mol L^{-1} for the ns and ps measurements at 532 nm, respectively; and 4.71×10^{-3} mol L^{-1} for the 680 nm measurement.

In the near-IR region, in which the ground-state absorption is extremely weak, the excited state is populated by

 © 2012 Wiley-VCH Verlag GmbH & Co. KGaA, Weinheim

Table 6. Excited-state absorption cross sections and TPA cross sections of **1** at selected wavelengths in CH_2Cl_2 solution.

λ [nm]	σ_0 10^{-18} cm^2	σ_S^c	σ_T	σ_S/σ_0	σ_T/σ_0	σ_2 [GM]
430	29.6	40	92[c]	1.4	3.1	–
475	14.3	30	101[c]	2.1	7.1	–
500	6.75	48	107[c]	7.1	15.9	–
532	1.48	40±5	103±10	27	69.6	–
550	1.25	40	115[c]	32	92	–
575	0.344	40	154[c]	116	448	–
600	0.0956	45	195[c]	471	2.04×10^3	–
630	0.0318	200	253[c]	6.29×10^3	7.96×10^3	–
680	0.01	180	148[c]	1.80×10^4	1.48×10^4	–
740	0[a]	40[b]	86[c]	–	–	600
800	0[a]	27[b]	89[c]	–	–	650
850	0[a]	–	–	–	–	1200[d]
875	0[a]	–	–	–	–	220[e]
910	0[a]	–	–	–	–	200[e]

[a] Approximate value. [b] $\sigma_S(\lambda)$ $\tilde{\nu}=$ are determined from the value σ_S-(532 nm) $=4.0\times10^{-17}$ cm^2 and the fs TA spectrum at zero time delay. Because the fs TA will include contributions from both S_1 and S_2, these values should be considered effective cross sections for the singlet excited states. [c] σ_T(532 nm) $=1.03\times10^{-16}$ cm^2 was determined from combined fitting of nanosecond and picosecond *Z*-scan data. For other wavelengths, $\sigma_T(\lambda)$ is determined from the value of σ_T(532 nm) and the fs TA spectrum at 5.8 ns time delay. [d] Effective TPA cross section for the *Z* scan of lowest energy (0.5 J cm^{-2}). *Z* scans at a progression of higher energies (0.7 and 1.1 J cm^{-2}) yield effective σ_2 values of 1900 GM and 2000 GM, respectively, clear evidence for two-photon-initiated excited-state absorption. [e] Effective TPA cross section for the *Z* scan of 0.3 J cm^{-2} fluence on axis.

TPA. The observed nonlinear absorption is thus two-photon-initiated excited-state absorption. The singlet and triplet excited-state absorption cross sections at 740 and 800 nm were estimated from the values at 532 nm and the fs TA spectra at zero and 5.8 ns time delays, respectively. These estimated values were used as parameters in the model and allowed the TPA cross sections at these wavelengths to be obtained by fitting the *Z*-scan data. At wavelengths of 850 nm and above, fs TA data were not available, so this method could not be used to provide an estimate of the excited-state absorption cross sections. As the relative contributions of two-photon and excited-state absorption cannot be unambiguously deconvolved for wavelengths of 850, 875, and 910 nm, the TPA cross sections given in Table 6 for these wavelengths represent effective values. Comparison of the deconvolved or the effective TPA cross sections of **1** in the spectral region of 630–910 nm with those of the other reported platinum complexes is provided in the Supporting Information, Table S6. It is clear that the TPA cross sections of **1** are among the largest values reported for platinum complexes.[5t,22]

Reverse saturable absorption: Both the fs and ns transient absorption measurements suggest that complex **1** exhibits stronger excited-state absorption than ground-state absorption in the visible-to-near-IR region. Therefore, reverse saturable absorption in this spectral region should occur. To demonstrate this, a nonlinear transmission experiment was carried out at 532 nm with 4.1 ns laser pulses. The result is shown in Figure 10. The transmission of the solution decreases drastically from 80% at low incident fluence to 24% at 1.8 J cm^{-2}. From the fractional populations of the affected excited states (bottom part of Figure 10) it is clear that the triplet excited state is the dominant contributor to the observed decrease in transmission. Because the triplet excited-state absorption cross section greatly exceeds that of the ground-state ($\sigma_T/\sigma_0=69.6$, see Table 6), strong reverse saturable absorption occurs.

Conclusion

A platinum(II) complex (**1**) with a new type of C^N^N ligand, that is, 6-(7-benzothiazol-2′-yl-9,9-diethyl-9*H*-fluoren-2-yl)-2,2′-bipyridine, was synthesized and the structure was characterized with spectroscopic techniques and single crystal X-ray crystallography. The C^N^N ligand forms a distorted square-planar configuration with the Pt^{II} ion. The resulting complex exhibits ligand-centered $^1\pi$–π^* transition in the UV and blue region, and a broad, structureless ^{1}MLCT/^{1}LLCT absorption band in the visible region; this is supported by DFT calculations. The emission of **1** at room temperature and at 77 K is dominated by $^3\pi$–π^* character, possibly mixed with some ^{3}MLCT character. The degree of

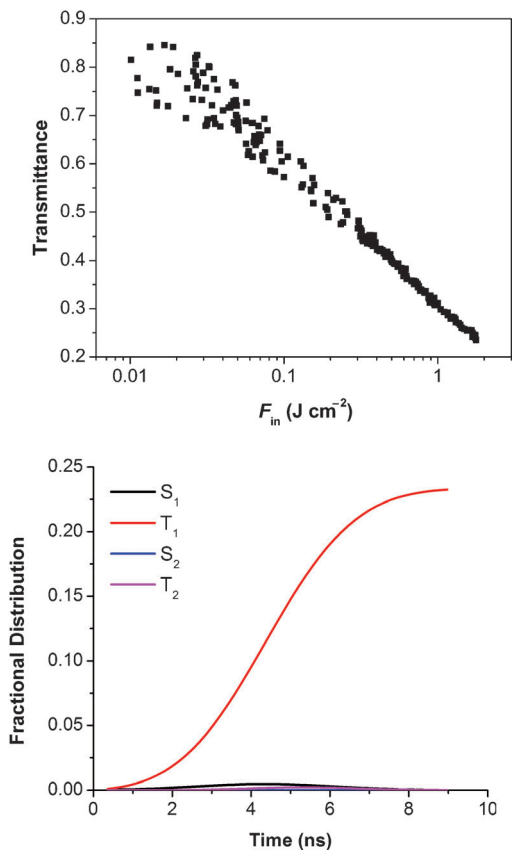

Figure 10. Top) Nonlinear transmission of **1** in CH_2Cl_2 solution for 4.1 ns laser pulses at 532 nm. The linear transmission is 80%, and the path length of the cuvette is 2 mm. Bottom) The fractional population of the affected excited states on the input face of the sample within a laser pulse. The fluence used for the calculation is 0.24 J cm^{-2}.

 © 2012 Wiley-VCH Verlag GmbH & Co. KGaA, Weinheim

$^3\pi$–π^* and ^{3}MLCT mixing varies in solvents with different polarities. In contrast, the excited state that gives rise to the transient absorption (both fs and ns TA) is predominantly the π–π^* state. *Z*-scan experiments with ns and ps laser pulses at 532 nm and ps laser pulses at a variety of visible and near-IR wavelengths reveal that complex **1** exhibits large ratios of excited-state absorption to ground-state absorption from 430 to 680 nm and strong TPA from 740 to 910 nm, which are among the largest values reported for platinum complexes. As one might expect from the large value of the ratio at 532 nm, strong reverse saturable absorption of ns laser pulses was observed at this wavelength. Therefore, complex **1** could potentially be used as a broadband nonlinear absorbing material.

Experimental Section

Synthesis: All solvents and reagents were purchased from Aldrich or Alfa Aesar and used as received, unless otherwise stated. 6-Bromo-2,2′-bipyridine (**6**),[23] 2,7-dibromo-9,9-diethyl-9*H*-fluorene (**2**),[24] 7-bromo-9,9-diethyl-9*H*-fluorene-2-carbaldehyde (**3**);[24] and 2-(7-bromo-9,9-diethyl-9*H*-fluoren-2-yl)-benzothiazole (**4**)[24] were prepared according to the procedures published in the literature. The procedures for the synthesis of **5**, **7**, **1-L**, and **1** are described below. Compounds **5**, **1-L**, and **1** were characterized by ^{1}H NMR spectroscopy and elemental analyses. Additional characterization by ESI-HRMS was carried out on **1-L** and **1**. ^{1}H NMR spectra were measured on a Varian Oxford-400 VNMR spectrometer or a Varian Oxford-500 VNMR spectrometer; and ESI-HRMS analyses were conducted on a Bruker Daltonics BioTOF III mass spectrometer. Elemental analyses were performed by NuMega resonance labs in San Diego, CA.

Compound 5: Compound **4** (3.05 g, 7.00 mmol) was dissolved in degassed dry THF (40 mL) and the solution was cooled down to −78 °C in a dry ice–heptane bath. *n*-Butyl lithium (5.1 mL) in hexane (1.60 M, 8.20 mmol) was then added dropwise under argon. After stirring for 30 min, isopropyl pinacolyl borate (1.70 mL, 1.52 g, 8.20 mmol,) was added with a syringe. The reaction mixture was stirred overnight, first at −78 °C and then slowly warmed up to room temperature. After reaction, the mixture was again cooled down to 5 °C, and treated with a hydrochloric acid solution (15 mL, 6.00 M). Then THF was removed by distillation, and the aqueous phase was extracted three times with diethyl ether (3×50 mL). The organic layer was washed with brine, dried with Na_2SO_4, and the solvent was removed. The residual solid was recrystallized from toluene to give 2.66 g yellow crystals (yield: 70 %). ^{1}H NMR ($CDCl_3$): δ = 8.13 (s, 1 H), 8.11 (d, *J* = 8.0 Hz, 1 H), 8.04 (d, *J* = 8.0 Hz, 1 H), 7.92 (d, *J* = 8.0 Hz, 1 H), 7.80–7.86 (m, 2 H), 7.74–7.80 (m, 2 H), 7.51 (t, *J* = 9.0 Hz, 1 H), 7.40 (t, *J* = 9.0 Hz, 1 H), 2.10–2.22 (m, 4 H), 1.40 (s, 12 H), 0.28–0.33 ppm (m, 6 H); elemental analysis calcd (%) for $C_{30}H_{32}BNO_2S$: C 74.8, H 6.7, N 2.9; found: C 74.8, H 7.1, N 3.2.

Compound 1-L: Compounds **5** (0.48 g, 1.00 mmol), **6** (0.35 g, 1.50 mmol), and K_2CO_3 (5.50 g, 0.04 mol) were dissolved in a mixed solvent of dioxane (40 mL), toluene (40 mL), and water (20 mL), and the solution was degassed with argon for 30 min. $[Pd(PPh_3)_4]$ (33 mg, 0.03 mmol) and PPh_3 (16 mg, 0.06 mmol) were then added. After refluxing for 72 h under argon, the aqueous phase was extracted with diethyl ether (3×50 mL). The organic layer was washed with brine, dried with Na_2SO_4, and the solvent was removed. The residual solid was purified by chromatography on silica gel (Sorbent Technologies, 60 Å, 230–450 mesh) column. The byproduct was removed first by toluene, then the desired product was obtained by using dichloromethane or ether as the eluent. The crude product was purified by recrystallization from dichloromethane and heptane to give colorless crystal (0.35 g, yield: 70 %) suitable for X-ray diffraction analysis. ^{1}H NMR ($CDCl_3$): δ = 8.72 (d, *J* = 4.0 Hz, 1 H), 8.70 (d, *J* = 8.0 Hz, 1 H), 8.44 (dd, *J* = 8.0 and 1.2 Hz, 1 H), 8.24 (d, *J* = 1.6 Hz, 1 H), 8.21 (dd, *J* = 8.0 and 1.6 Hz, 1 H), 8.20 (s, 1 H), 8.14 (d, *J* = 8.0 Hz, 1 H), 8.05 (dd, *J* = 8.0 and 1.6 Hz, 1 H), 7.79–7.90 (m, 6 H), 7.47 (dt, *J* = 8.0 and 1.2 Hz, 1 H), 7.36 (dt, *J* = 8.0 and 1.2 Hz, 1 H), 7.26–7.32 (m, 1 H), 2.20–2.28 (m, 4 H), 0.46 ppm (t, *J* = 7.6 Hz, 6 H); ESI-HRMS: *m/z*: calcd for $[C_{34}H_{27}N_3S+H]^+$: 510.1998; found: 510.1980; elemental analysis calcd (%) for $C_{34}H_{27}N_3S$: C 80.12, H 5.34, N 8.24; found: C 79.85, H 5.66, N 8.40.

Compound 7: Ligand **1-L** (130 mg, 0.26 mmol) and $[Pt(DMSO)_2Cl_2]$ (126 mg, 0.30 mmol) were dissolved in DMF (5 mL) with a few drops of water. The solution was stirred at 80 °C for 30 h under argon. The formed yellow solid was collected by filtration, washed with water, methanol and ether, and dried in vacuum. The crude product of **7** (190 mg) was obtained in a quantitative yield. Due to the poor solubility of **7** (insoluble in ethanol, ether, hexane and toluene, slightly soluble in DMSO, DMF and CH_2Cl_2), it could not be further purified by column chromatography or recrystallization. Therefore, it was used directly in the following step for preparation of **1** without further purification and/or characterization.

Compound 1: To a degassed suspension of **7** (128 mg, 0.16 mmol) and 1-ethynyl-4-methylbenzene (23 mg, 0.20 mmol, 25 μL) in DMF (70 mL), powder KOH (14 mg, 0.25 mmol), and a catalytic amount of CuI were added. The reaction mixture was heated and stirred at 80 °C for 48 h under argon. After removing the solvent, the residue was washed with water and ether, dried in vacuum, and purified by column chromatography on silica gel (Sorbent Technologies, 60 Å, 230–450 mesh) column. Dichloromethane with 3 % methanol (v/v) was used as the eluent. The pure product of complex **1** was obtained as an orange solid (44 mg, yield: 31 %). ^{1}H NMR (500 MHz, $CDCl_3$): δ = 9.24 (s, 1 H), 8.44 (t, *J* = 42 Hz, 1 H), 8.15 (d, *J* = 1.5 Hz, 1 H), 8.12 (d, *J* = 8.0 Hz, 1 H), 8.03 (dd , *J* = 8.0 and 1.5 Hz, 1 H), 8.01 (d, *J* = 10 Hz, 1 H), 7.88–7.96 (m, 3 H), 7.82 (t, *J* = 8.0 Hz, 1 H), 7.63 (br s, 1 H), 7.57 (d, *J* = 8.0 Hz, 1 H), 7.52 (dt, *J* = 8.0 and 1.0 Hz, 3 H), 7.48 (dt, *J* = 8.0 and 1.0 Hz, 1 H), 7.36 (dt, *J* = 8.0 and 1.0 Hz, 1 H), 7.33 (s, 1 H), 7.18 (d, *J* = 8.0 Hz, 2 H), 2.37 (s, 3 H), 2.06–2.26 (m, 4 H), 0.43 ppm (t, *J* = 7.5 Hz, 6 H); ESI-HRMS: *m/z*: calcd for $[C_{43}H_{33}N_3PtS+H]^+$: 819.2119; found, 819.2105; elemental analysis calcd (%) for $C_{43}H_{33}N_3PtS{\cdot}CH_2Cl_2$: C 58.47, H 3.90, N 4.65; found: C 58.33, H 3.93, N 4.91.

Crystal structure determination: Single crystals of **1-L** and **1** were obtained by slow diffusion of heptane into dilute dichloromethane solutions of the sample. The single crystal X-ray data were collected on a SIEMENS diffractometer with a 1K CCD area detector (graphite-monochromated $Mo_{K\alpha}$ radiation) at ambient temperature. The structures were solved by direct methods and refined on F_2 by using the SHELXTL V6.14 package (after absorption corrections with SADABS). All of the non-hydrogen atoms were refined with anisotropic displacement coefficients. Hydrogen atoms were idealized using the SHELXTL software. Details of the data collections and refinements are given in Table 7.

Computational details for DFT calculations: DFT calculations were performed for complex **1** to characterize the FMOs, and to understand the nature of the ground and low-lying, excited, electronic states. The low-lying, excited, electronic states were characterized by performing TDDFT calculations.[25] A hybrid generalized gradient approximation (hybrid GGA) exchange-correlation functional was used for all DFT calculations. The particular hybrid GGA used is known by the acronym MPW3LYP, which consists of the three-parameter modified Perdew-Wang (MPW) exchange functional and the Lee–Yang–Parr (LYP) correlation functional.[26] The basis sets used include functions from the LANL2DZ set[27] and from the 6–31G* set;[28] the particular combination is abbreviated in this work as LANG631. LANL2DZ is an effective core potential (ECP) basis set and was used to describe the platinum atom; this provides some correction for scalar relativistic effects of the platinum atom. The 6–31G* basis set was used for the descriptions of all other atoms.

Full geometry optimizations were performed for the ground state of complex **1** and excited singlet electronic states were calculated at the ground-state-optimized geometry by using the TDDFT method, with the MPW3LYP exchange-correlation functional. The Gaussian 03 (revision C.02) software suite,[29] running on a 96-node distributed-memory

 © 2012 Wiley-VCH Verlag GmbH & Co. KGaA, Weinheim

Table 7. Single-crystal X-ray parameters and refinement data for **1-L** and **1**.

	1-L	**1**
T [K]	273(2)	273(2)
λ [Å]	0.71073	0.71073
formula	$C_{34}H_{27}N_3S$	$C_{43}H_{33}N_3PtS$
M_r	509.65	818.87
crystal size [mm]	$0.66\times0.3\times0.26$	$0.22\times0.16\times0.06$
crystal system	monoclinic	triclinic
space group	$C2/c$	$P\bar{1}$
a [Å]	34.358(4)	7.527(7)
b [Å]	7.4355(9)	13.206(12)
c [Å]	24.366(3)	17.357(15)
α [°]	90	84.284(16)
β [°]	120.523(2)	84.008(16)
γ [°]	90	86.178(15)
V [Å^3]	5362.00(11)	1705(3)
Z	8	2
ρ_{calc} [g cm^{-3}]	1.263	1.595
μ [mm^{-1}]	0.149	4.213
F(000)	2144	812
reflns collected	14846	15113
unique reflections	5243	7320
no. of reflns ($I\geq2\sigma$)	3469	5879
goodness-of-fit on F^2	1.006	1.076
2θ max [°]	52	52
R_1/wR_2 ($I\geq2\sigma(I)$)[a]	0.0468/0.1422	0.0464/0.1362
R_1/wR_2 (all data)[a]	0.0797/0.1721	0.0668/0.1757

[a] $R_1=\Sigma||F_o|-|F_c||/\Sigma|F_o|$, $wR_2=[\Sigma(w(F_o^2-F_c^2)^2)/\Sigma w(F_o^2)^2]^{1/2}$ for $F_o^2>2\sigma(F_o^2)$, $w=1/[\sigma^2(F_o^2)+(AP)^2+BP]$, for which $P=(F_o^2+2F_c^2)/3$; A(B) = 0.19323 (0.000) for **1-L** and A(B) = 0.1176 (0.000) for **1**.

cluster with 192 Dual 3.06 GHz Xeon-HT processors at North Dakota State University, was used to perform all calculations.

Photophysical measurements: The UV/Vis spectra of **1-L** and **1** in different solvents (spectrophotometric grade) were acquired by using a UV-2501 spectrophotometer. The steady-state emission spectra in different solvents were obtained on a SPEX fluorolog-3 fluorometer/phosphorometer. The emission quantum yields were measured by the relative actinometry method[30] in degassed solutions. A degassed aqueous solution of $[Ru(bpy)_3]Cl_2$ ($\Phi_{em}=0.042$, $\lambda_{ex}=436$ nm)[31] was used as the reference for complex **1** and an aqueous solution of quinine sulfate ($\Phi_f=0.546$, $\lambda_{ex}=347.5$ nm)[32] was used as the reference for ligand **1-L**. The excited-state lifetimes, the triplet TA spectra, and the triplet excited-state quantum yields were measured on an Edinburgh LP920 laser flash photolysis spectrometer. The third harmonic output (355 nm) of a Nd:YAG laser (Quantel Brilliant, pulsewidth ca. 4.1 ns, repetition rate is set to 1 Hz) was used as the excitation source. Sample solutions were purged with Ar for 30 min prior to each measurement. The femtosecond transient difference absorption spectra and the singlet excited-state lifetime were measured with a femtosecond pump-probe UV/Vis spectrometer (HELIOS) manufactured by Ultrafast Systems LLC. The sample solution in a 2 mm cuvette was excited at 400 nm by using a 150 fs Ti:Sapphire laser (Spectra Physics Hurricane, 1 kHz repetition rate, 1 mJ per pulse at 800 nm) and the absorption was probed from 425 to 800 nm with sapphire generated white-light continuum.

The triplet excited-state molar extinction coefficients (ε_T) at the TA band maximum were determined by the singlet depletion method,[15] in which the following equation was used to calculate the ε_T:[15]

$$\varepsilon_T=\frac{\varepsilon_S[\Delta OD_T]}{\Delta OD_S}$$

in which ΔOD_S and ΔOD_T are the optical-density changes at the minimum of the bleaching band and at the maximum of the positive band in the TA spectrum, respectively, and ε_S is the ground-state molar extinction coefficient at the wavelength of the bleaching band minimum. After obtaining the ε_T value, the triplet excited-state quantum yield was measured by relative actinometry,[16] in which SiNc in benzene was used as the reference ($\varepsilon_{590}=70000\,M^{-1}cm^{-1}$, $\Phi_T=0.20$).[33]

Nonlinear optical characterizations: The nonlinear absorption of complex **1** was characterized by open-aperture Z-scan experiments by using ns laser at 532 nm and ps laser from 450 to 900 nm, and by nonlinear-transmission experiments at 532 nm by using ns laser. For the open-aperture Z-scan measurements, the experimental setup and experimental details were similar to those reported in our previous publications.[5s,20] The experimental data were fitted by using a five-level model to extract the excited-state absorption cross sections and the TPA cross sections. The details of the model and fitting procedure were the same as those reported previously.[5s,20]

The nonlinear-transmission experiment for complex **1** was conducted in CH_2Cl_2 in a 2 mm cuvette by using 4.1 ns laser pulses at 532 nm. The light source was a Quantel Brilliant ns laser with a repetition rate of 10 Hz. The experimental setup and details are the same as previously described.[5c] A 20 cm plano-convex lens was used to focus the beam to the 2 mm thick sample cuvette. The linear transmission of the solution was adjusted to 80% at 532 nm.

Acknowledgements

This work is supported by National Science Foundation (CAREER CHE-0449598 and CHEM-0946990) and the Army Research Laboratory (W911NF-06–2–0032).

[1] a) W. Lu, B. X. Mi, M. C. W. Chan, Z. Hui, C. M. Che, N. Zhu, S. T Lee, *J. Am. Chem. Soc.* **2004**, *126*, 4958–4971; b) H. Yersin, D. Donges, W. Humbs, J. Strasser, R. Sitters, M. Glasbeek, *Inorg. Chem.* **2002**, *41*, 4915–4922; c) J. Brooks, Y. Babayan, S. Lamansky, P. I. Djurovich, I. Tsyba, R. Bau, M. E. Thompson, *Inorg. Chem.* **2002**, *41*, 3055–3066; d) J. C. Shi, H. Y. Chao, W. F. Fu, S. M. Peng, C. M. Che, *J. Chem. Soc. Dalton Trans.* **2000**, 3128–3132; e) L. Chassot, A. von Zelewsky, D. Sandrini, M. Maestri, V. Balzani, *J. Am. Chem. Soc.* **1986**, *108*, 6084–6085; f) M. Maestri, D. Sandrini, V. Balzani, L. Chassot, P. Jolliet, A. von Zelewsky, *Chem. Phys. Lett.* **1985**, *122*, 375–379; g) W. Y. Wong, Z. He, S. K. So, K. L. Tong, Z. Lin, *Organometallics* **2005**, *24*, 4079–4082; h) S. C. F. Kui, I. H. T. Sham, C. C. C. Cheung, C. W. Ma, B. Yan, N. Zhu, C. M. Che, W. F. Fu, *Chem. Eur. J.* **2007**, *13*, 417–435; i) S. C. Chan, M. C. W. Chan, Y. Wang, C. M. Che, K. K. Cheung, N. Zhu, *Chem. Eur. J.* **2001**, *7*, 4180–4190.

[2] a) T. J. Wadas, S. Chakraborty, R. J. Lachicotte, Q. M. Wang, R. Eisenberg, *Inorg. Chem.* **2005**, *44*, 2628–2638; b) S. Chakraborty, T. J. Wadas, H. Hester, C. Flaschenreim, R. Schmehl, R. Eisenberg, *Inorg. Chem.* **2005**, *44*, 6865–6878; c) E. C. H. Kwok, M. Y. Chan, K. M. C. Wong, W. H. Lam, V. W. W. Yam, *Chem. Eur. J.* **2010**, *16*, 12244–12254.

[3] a) M. Hissler, J. E. McGarrah, W. B. Connick, D. K. Geiger, S. D. Cummings, R. Eisenberg, *Coord. Chem. Rev.* **2000**, *208*, 115–137; b) J. E. McGarrah, Y. J. Kim, M. Hissler, R. Eisenberg, *Inorg. Chem.* **2001**, *40*, 4510–4511.

[4] a) Q.-Z. Yang, L.-Z. Wu, H. Zhang, B. Chen, Z.-X. Wu, L.-P. Zhang, Z.-H. Tung, *Inorg. Chem.* **2004**, *43*, 5195–5197; b) L. Z. Wu, T. C. Cheung, C. M. Che, K. K. Cheung, M. H. W. Lam, *Chem. Commun.* **1998**, 1127–1128; c) K.-H. Wong, M. C.-W. Chan, C. M. Che, *Chem. Eur. J.* **1999**, *5*, 2845–2849; d) S. C. F. Kui, S. S.-Y. Chui, C.-M. Che, N. Zhu, *J. Am. Chem. Soc.* **2006**, *128*, 8297–8309; e) K. M.-C. Wong, W.-S. Tang, X.-X Lu, N. Zhu, V. W.-W. Yam, *Inorg. Chem.* **2005**, *44*, 1492–1498; f) P. Du, J. Schneider, W. W. Brennessel, R. Eisenberg, *Inorg. Chem.* **2008**, *47*, 69–77; g) W. Lu, M. C. W. Chan, N. Zhu, C.-M. Che, Z. He, K. Y. Wong, *Chem. Eur. J.* **2003**, *9*, 6155–6166; h) I. Mathew, W. Sun, *Dalton Trans.* **2010**, *39*, 5885–5898; i) H. Zhang, B. Zhang, Y. Li, W. Sun, *Inorg. Chem.* **2009**, *48*, 3617–3627; j) Z. Ji, Y. Li, W. Sun, *J. Organomet. Chem.* **2009**, *694*, 4140–4145.

 © 2012 Wiley-VCH Verlag GmbH & Co. KGaA, Weinheim

[5] a) W. Sun, Z. Wu, Q. Yang, L. Wu, C. Tung, *Appl. Phys. Lett.* **2003**, *82*, 850–852; b) F. Guo, W. Sun, Y. Liu, K. Schanze, *Inorg. Chem.* **2005**, *44*, 4055–4065; c) W. Sun, H. Zhu, P. M. Barron, *Chem. Mater.* **2006**, *18*, 2602–2610; d) P. Shao, Y. Li, W. Sun, *J. Phys. Chem. A* **2008**, *112*, 1172–1179; e) G.-J. Zhou, W.-Y. Wong, D. Cui, C. Ye, *Chem. Mater.* **2005**, *17*, 5209–5217; f) F. Guo, W. Sun, *J. Phys. Chem. B* **2006**, *110*, 15029–15036; g) T. M. Pritchett, W. Sun, F. Guo, B. Zhang, M. J. Ferry, J. E. Rogers-Haley, W. Shensky III, A. G. Mott, *Opt. Lett.* **2008**, *33*, 1053–1055; h) P. Shao, Y. Li, W. Sun, *Organometallics* **2008**, *27*, 2743–2749; i) Z. Ji, Y. Li, W. Sun, *Inorg. Chem.* **2008**, *47*, 7599–7607; j) P. Shao, W. Sun, *Inorg. Chem.* **2007**, *46*, 8603–8612; k) Y. Li, T. M. Pritchett, P. Shao, J. E. Haley, H. Zhu, W. Sun, *J. Organomet. Chem.* **2009**, *694*, 3688–3691; l) P. Shao, Y. Li, A. Azenkeng, M. Hoffmann, W. Sun, *Inorg. Chem.* **2009**, *48*, 2407–2419; m) W. Sun, Y. Li, T. M. Pritchett, Z. Ji, J. E. Haley, *Nonlinear Opt., Quantum Opt.* **2010**, *40*, 163–174; n) T. M. Pritchett, W. Sun, B. Zhang, M. J. Ferry, Y. Li, J. E. Haley, D. Mackie, W. Shensky, A. G. Mott, *Opt. Lett.* **2010**, *35*, 1305–1307; o) J. Yi, B. Zhang, P. Shao, Y. Li, W. Sun, *J. Phys. Chem. A* **2010**, *114*, 7055–7062; p) R. Liu, Y. Li, H. Zhu, W. Sun, *J. Phys. Chem. A* **2010**, *114*, 12639–12645; q) W. Sun, B. Zhang, Y. Li, T. M. Pritchett, Z. Li, J. E. Haley, *Chem. Mater.* **2010**, *22*, 6384–6392; r) P. Shao, Y. Li, J. Yi, T. M. Pritchett, W. Sun, *Inorg. Chem.* **2010**, *49*, 4507–4517; s) Z. Ji, Y. Li, T. M. Pritchett, N. S. Makarov, J. E. Haley, Z. Li, M. Drobizhev, A. Rebane, W. Sun, *Chem. Eur. J.* **2011**, *17*, 2479–2491; t) J. E. Rogers, J. E. Slagle, D. M. Krein, A. R. Burke, B. C. Hall, A. Fratini, D. G. McLean, P. A. Fleitz, T. M. Cooper, M. Drobizhev, N. S. Makarov, A. Rebane, K.-Y. Kim, R. Farley, K. S Schanze, *Inorg. Chem.* **2007**, *46*, 6483–6494.

[6] a) J. A. G. Williams, *Top. Curr. Chem.* **2007**, *281*, 205–268; b) I. Eryazici, C. N. Moorefield, G. R. Newkome, *Chem. Rev.* **2008**, *108*, 1834–1895; c) R. McGuire Jr, M. C. McGuire, D. R. McMillin, *Coord. Chem. Rev.* **2010**, *254*, 2574–2583.

[7] M. Pawlicki, H. A. Collins, R. G. Denning, H. L. Anderson, *Angew. Chem.* **2009**, *121*, 3292–3316; *Angew. Chem. Int. Ed.* **2009**, *48*, 3244–3266.

[8] a) B. Li, J. Li, Y. Fu, Z. Bo, *J. Am. Chem. Soc.* **2004**, *126*, 3430–3431; b) F. Wang, G. C. Bazan, *J. Am. Chem. Soc.* **2006**, *128*, 15786–15792; c) J. Ding, M. Day, G. Robertson, J. Roovers, *Macromolecules* **2002**, *35*, 3474–3483; d) D. S. Chung, S. J. Lee, J. W. Park, D. B. Choi, D. H. Lee, J. W. Park, S. C. Shin, Y.-H. Kim, S.-K. Kwon, C. E. Park, *Chem. Mater.* **2008**, *20*, 3450–3456.

[9] R. McGuire, M. H. Wilson, J. J. Nash, P. E. Fanwick, D. R. McMillin, *Inorg. Chem.* **2008**, *47*, 2946–2948.

[10] S. Diring, P. Retailleau, R. Ziessel, *J. Org. Chem.* **2007**, *72*, 10181–10193.

[11] a) W. Lu, M. C. W. Chan, N. Zhu, C. M. Che, C. Li, Z. Hui, *J. Am. Chem. Soc.* **2004**, *126*, 7639–7651; b) T.-C. Cheung, K.-K. Cheung, S.-M. Peng, C. M. Che, *J. Chem. Soc. Dalton Trans.* **1996**, 1645–1651; c) A. R. Dick, J. W. Kampf, M. S. Sanford, *Organometallics* **2005**, *24*, 482–485.

[12] V. M. Miskowski, V. H. Houlding, *Inorg. Chem.* **1991**, *30*, 4446–4452.

[13] A. E. Reed, L. A. Curtiss, F. Weinhold, *Chem. Rev.* **1988**, *88*, 899–926.

[14] a) A. Juris, V. Balzani, F. Barigelletti, S. Campagna, P. Belser, A. Von Zelewsky, *Coord. Chem. Rev.* **1988**, *84*, 85–277; b) S. D. Cummings, R. Eisenberg, *J. Am. Chem. Soc.* **1996**, *118*, 1949–1960; c) A. S. Polo, M. K. Itokazu, K. M. Frin, A. O. de T. Patrocinio, N. Y. M. Iha, *Coord. Chem. Rev.* **2006**, *250*, 1669–1680; d) S.-W. Lai, M. C. W. Chan, K.-K. Cheung, C.-M. Che, *Inorg. Chem.* **1999**, *38*, 4262–4267.

[15] I. Carmichael, G. L. Hug, *J. Phys. Chem. Ref. Data* **1986**, *15*, 1–250.

[16] C. V. Kumar, L. Qin, P. K. Das, *J. Chem. Soc. Faraday Trans. 2* **1984**, *80*, 783–793.

[17] J. E. Rogers-Haley, J. L. Monahan, D. M. Krein, J. E. Slagler, D. G. McLean, T. M. Cooper, A. M. Urbas, *Proc. SPIE* **2008**, *7049*, 704 906.

[18] J. V. Caspar, T. J. Meyer, *J. Phys. Chem.* **1983**, *87*, 952–957.

[19] M. Sheik-Bahae, A. A. Said, T.-H. Wei, D. J. Hagen, E. W. V. Stryland, *IEEE J. Quantum Electron.* **1990**, *26*, 760–769.

[20] Y. Li, T. M. Pritchett, J. Huang, M. Ke, P. Shao, W. Sun, *J. Phys. Chem. A* **2008**, *112*, 7200–7207.

[21] a) T. J. McKay, J. Staromlynska, J. R. Davy, J. A. Bolger, *J. Opt. Soc. Am. B* **2001**, *18*, 358–362; b) S. Guha, K. Kang, P. Porter, J. E. Roach, D. E. Remy, F. J. Aranda, D. V. G. L. N. Rao, *Opt. Lett.* **1992**, *17*, 264–266; c) J. W. Perry, K. Mansour, I.-Y. S. Lee, X.-L. Wu, P. V. Bedworth, C.-T. Chen, D. Ng, S. R. Marder, P. Miles, T. Wada, M. Tian, H. Sasabe, *Science* **1996**, *273*, 1533–1536; d) Y. Song, G. Fang, Y. Wang, S. Liu, C. Li, *Appl. Phys. Lett.* **1999**, *74*, 332–334; e) M. Pittman, P. Plaza, M. M. Martin, Y. H. Meyer, *Opt. Commun.* **1998**, *158*, 201–212; f) J. Si, M. Yang, Y. Wang, L. Zhang, C. Li. D. Wang, S. Dong, W. Sun, *Appl. Phys. Lett.* **1994**, *64*, 3083–3085.

[22] a) C. K. M. Chan, C.-H. Tao, H.-L. Tam, N. Zhu, V. W.-W. Yam, K.-W. Cheah, *Inorg. Chem.* **2009**, *48*, 2855–2864; b) E. Glimsdal, M. Carlsson, B. Eliasson, B. Minaev, M. Lindgren, *J. Phys. Chem. A* **2007**, *111*, 244–250; c) R. Westlund, E. Glimsdal, M. Lindgren, R. Vestberg, C. Hawker, C. Lopez, E. Malmström, *J. Mater. Chem.* **2008**, *18*, 166–175.

[23] D. Shin, C. Switzer, *Chem. Commun.* **2007**, 4401–4403.

[24] R. Kannan, G. S. He, L. Yuan, F. Xu, P. N. Prasad, A. G. Dombroskie, B. A. Reinhardt, J. W. Baur, R. A. Vaia, L.-S. Tan, *Chem. Mater.* **2001**, *13*, 1896–1904.

[25] a) R. E. Stratmann, G. E. Scuseria, M. J. Frisch, *J. Chem. Phys.* **1998**, *109*, 8218–8224; b) R. Bauernschmitt, R. Ahlrichs, *Chem. Phys. Lett.* **1996**, *256*, 454–464; c) M. E. Casida, C. Jamorski, K. C. Casida, D. R. Salahub, *J. Chem. Phys.* **1998**, *108*, 4439–4449.

[26] Y. Zhao, D. G. Truhlar, *J. Phys. Chem. A* **2004**, *108*, 6908–6918.

[27] a) P. J. Hay, W. R. Wadt, *J. Chem. Phys.* **1985**, *82*, 270–283; b) W. R. Wadt, P. J. Hay, *J. Chem. Phys.* **1985**, *82*, 284–298; c) P. J. Hay, W. R. Wadt, *J. Chem. Phys.* **1985**, *82*, 299–310.

[28] a) P. C. Hariharan, J. A. Pople, *Theor. Chim. Acta* **1973**, *28*, 213–222; b) M. M. Francl, W. J. Petro, W. J. Hehre, J. S. Binkley, M. S. Gordon, D. J. DeFrees, J. A. Pople, *J. Chem. Phys.* **1982**, *77*, 3654–3665; c) T. Clark, J. Chandrasekhar, P. V. R. Schleyer, *J. Comput. Chem.* **1983**, *4*, 294–301; d) R. Krishnan, J. S. Binkley, R. Seeger, J. A. Pople, *J. Chem. Phys.* **1980**, *72*, 650–654; e) P. M. W. Gill, B. G. Johnson, J. A. Pople, M. J. Frisch, *Chem. Phys. Lett.* **1992**, *197*, 499–505.

[29] Gaussian 03, Revision C.02, M. J. Frisch, G. W. Trucks, H. B. Schlegel, G. E. Scuseria, M. A. Robb, J. R. Cheeseman, J. A. Montgomery, Jr., T. Vreven, K. N. Kudin, J. C. Burant, J. M. Millam, S. S. Iyengar, J. Tomasi, V. Barone, B. Mennucci, M. Cossi, G. Scalmani, N. Rega, G. A. Petersson, H. Nakatsuji, M. Hada, M. Ehara, K. Toyota, R. Fukuda, J. Hasegawa, M. Ishida, T. Nakajima, Y. Honda, O. Kitao, H. Nakai, M. Klene, X. Li, J. E. Knox, H. P. Hratchian, J. B. Cross, V. Bakken, C. Adamo, J. Jaramillo, R. Gomperts, R. E. Stratmann, O. Yazyev, A. J. Austin, R. Cammi, C. Pomelli, J. W. Ochterski, P. Y. Ayala, K. Morokuma, G. A. Voth, P. Salvador, J. J. Dannenberg, V. G. Zakrzewski, S. Dapprich, A. D. Daniels, M. C. Strain, O. Farkas, D. K. Malick, A. D. Rabuck, K. Raghavachari, J. B. Foresman, J. V. Ortiz, Q. Cui, A. G. Baboul, S. Clifford, J. Cioslowski, B. B. Stefanov, G. Liu, A. Liashenko, P. Piskorz, I. Komaromi, R. L. Martin, D. J. Fox, T. Keith, M. A. Al-Laham, C. Y. Peng, A. Nanayakkara, M. Challacombe, P. M. W. Gill, B. Johnson, W. Chen, M. W. Wong, C. Gonzalez, J. A. Pople, Gaussian, Inc., Wallingford CT, **2004**.

[30] J. N. Demas, G. A. Crosby, *J. Phys. Chem.* **1971**, *75*, 991–1024.

[31] J. Van Houten, R. Watts, *J. Am. Chem. Soc.* **1976**, *98*, 4853–4858.

[32] D. F. Eaton, *Pure Appl. Chem.* **1988**, *60*, 1107–1114.

[33] P. A. Firey, W. E. Ford, J. R. Sounik, M. E. Kenney, M. A. J. Rodgers, *J. Am. Chem. Soc.* **1988**, *110*, 7626–7630.

Received: October 4, 2011
Published online: March 8, 2012

 © 2012 Wiley-VCH Verlag GmbH & Co. KGaA, Weinheim